Received: 20 January 2022 | Revised: 10 August 2022 | Accepted: 8 September 2022

DOI: 10.4218/etrij.2022-0011

ORIGINAL ARTICLE

ETRI Journal WILEY

Thermally reused solar energy harvesting using current mirror cells

Mostafa Noohi[1] | **Ali Mirvakili**[1] | **Hadi Safdarkhani**[1] | **Sayed Alireza Sadrossadat**[2]

[1]Department of Electrical Engineering, Yazd University, Yazd, Iran

[2]Department of Computer Engineering, Yazd University, Yazd, Iran

Correspondence
Ali Mirvakili, Department of Electrical Engineering, Yazd University, University Blvd, Safayieh, Yazd, Iran.
Email: ali.mirvakili@yazd.ac.ir

Abstract

This paper implements a simultaneous solar and thermal energy harvesting system, as a hybrid energy harvesting (HEH) system, to convert ambient light into electrical energy through photovoltaic (PV) cells and heat absorbed in the body of PV cells. Indeed, a solar panel equipped with serially connected thermoelectric generators not only converts the incoming light into electricity but also takes advantage of heat emanating from the light. In a conventional HEH system, the diode block is used to provide the path for the input source with the highest value. In this scheme, at each time, only one source can be handled to generate its output, while other sources are blocked. To handle this challenge of combining resources in HEH systems, this paper proposes a method for collecting all incoming energies and conveying its summation to the load via the current mirror cells in an approach similar to the maximum power point tracking. This technique is implemented using off-the-shelf components. The measurement results show that the proposed method is a realistic approach for supplying electrical energy to wireless sensor nodes and low-power electronics.

KEYWORDS

current mirror, hybrid energy harvesting, solar energy, supercapacitor, thermoelectric generator

1 | INTRODUCTION

Energy harvesting (EH) is the process of extracting energy from the environment and converting it into electrical energy and is a growing trend especially in the small-scale energy sector [1]. This energy, which comes from the energy sources that exist in the environment or the human body, is a renewable and clean energy [2]. The term EH is usually used for low powers in a range of about μW to mW [1]. These extracted powers are based on energy sources, such as mechanical vibrations [3], thermal [4], solar [5], biochemical [6], and radio waves [7]. In fact, EH technology is being used as a replacement for batteries in low-power electronic devices [8]. Likewise, due to the unpredictable performance and limited battery life in wireless sensor networks (WSNs), EH techniques have turned a typical battery-powered WSN into an autonomous WSN [9]. In addition to WSNs, EH systems can also be applied for providing a power supply for the Internet of Things (IoT) devices to achieve a stable

performance without the need of power cords, batteries, or chargers [10]. It is also important to note that hybrid EH (HEH) is turning to the point where it can be considered as a means of realizing the sustainable systems. Indeed, the extraction of energy from HEH sources prevents environmental degradation and facilitates the utilization of sustainable energies [11]. As a case in point, in Komiyama and Fujii [12], different types of energy sources that can be utilized in an electric vehicle are discussed, which not only provides clean energies but also reduces the environmental pollution. Although the single use of energy sources in small-scale EH applications is a solution to power wireless sensor nodes [13], there is a challenge in a number of applications, that is, the continuous supply of highly reliable electrical power. This is mainly due to the alternating nature of the environmental energy sources. Moreover, the HEH technique is used to ensure permanent access to electrical energy, and this is what was used in this article. By doing this, more energy can be extracted concurrently. Grasping a high efficiency is very important in EH systems. One solution is to use maximum power point tracking (MPPT) and impedance matching between the supply and the source. In this manner, the maximum power point (MPP) is the point that indicates the maximum output power [14]. Therefore, in an HEH system, the impedance matching of the harvester and the circuit must be observed to achieve higher efficiency. In addition, the MPPT system must be able to combine several sources of harvesting power to form a high-efficiency energy source. Moreover, the composition of the energy harvesters is also vital in an HEH system. For this purpose, four models [6] have been reported. In the first type, two different EH sources are used in an identical platform [15, 16]. In the second type, a multiplexer structure is used to switch between different EH sources [17, 18]. In the third type, separate converters are used for each EH source [14]. Finally, in the fourth type, energy harvesters are connected in a series-parallel configuration [6].

Several approaches of combining energy sources via HEH are reported. In Mohamad and others [19], a research work on a hybrid energy harvester with radio frequency and thermal and vibration sources for semi-active radio frequency identification (RFID) tags is presented. In Lee and others [20], a floating device with multifunctional EH technology using solar and thermal energy sources that can be used to power a wireless sensor node is reported. In Tan and Panda [21], an HEH technique to capture indoor light energy and thermal energy with only one energy management circuit for both energy sources is introduced to extend the lifetime of the wireless sensor node. In Kang and others [22], an energy combiner is provided to simultaneously deliver electrical energy extracted from individual energy separators to an energy storage device, which can be used as a subsystem. In Altinel and Kurt [23], potential energy models for IoT nodes are described by an HEH technique, and the energies harvested at the output of the EH modules are modeled using Gaussian mixture models. In Tanaka and others [24], an integrated system, which converts vibrational energy into electrical energy by multiple piezoelectric elements, is introduced. In Deng and others [25], an HEH system is used to extend the lifetime of the wireless sensor node in the field. The platform includes a multipurpose EH module to collect wind, solar radiation, and heat energy from the environment.

In this paper, the HEH system uses a combination of solar and thermal energy sources. In this system, a photovoltaic (PV) cell is taken to convert natural and artificial light into electrical energy, and the thermoelectric generator (TEG) is used to convert the temperature difference generated on the PV cell surface and air into electrical energy. Indeed, the idea is to reuse the heat generated at the surface of PV cells that are originally used to harvest the light and not the thermal energy. The combination of these energy sources at the input stage offers maximization of the received power with minimum losses, a known trend on increasing the efficiency of the system. To achieve this, this paper proposes the utilization of current mirror circuit to concurrently harvest both energy sources. Indeed, this method is regarded as the counterpart of the MPPT and is applicable for multisource EH systems. It is worth mentioning that the conventional method of implementing HEH system is based on using a diode block, which conducts a unique path only from the input with higher harvested energy to the output. In other words, in this conventional scheme, summation of incoming harvested energies will not be provided at the output node. The proposed method is able to alleviate this problem. The rest of this paper is organized as follows. Section 2 describes HEH system composed of solar and thermal EH sources and explains the DC-to-DC converter suitable for such an EH system. Section 3.3 provides the proposed method of combining the harvested energies from thermal and solar energy sources based on incorporating the current mirror circuit. Section 4 presents the experimental results. Eventually, Section 5 concludes this paper.

2 | DESCRIPTION OF HEH SYSTEM

It is intended to design and implement an HEH system for a wireless sensor node that is located in remote and hard to access environments, such as the ocean,

mountains, and forests. Therefore, the single use of energy to be extracted is not sufficient to provide the required power in such scenarios. Indeed, the harvesting power from multiple sources must be reached at the desired amount to act as a charger or battery complement in the wireless sensor node. A combination of solar and thermal energies is a promising method to accomplish this target.

2.1 | Solar EH system

Light is one of the most popular sources of renewable energies and is also widely used in EH techniques [26]. It can be produced from natural (solar) or artificial (lamp) sources. Wafer-based silicon technology is used in a high percentage of most solar cells on the world market [27]. Wafers with thicknesses of lower than 200 μm are made of monocrystalline silicon (c-Si) and polycrystalline silicon (pc-Si). Monocrystalline solar cells are made of single crystals of silicon. On the other hand, polycrystalline PV modules are composed of a number of different crystals that are connected to each other in a cell. In general, monocrystalline cells are more efficient than polycrystalline cells [28]. In this paper, the SP5V400 solar panel, which has a monocrystalline structure, is used to convert solar energy into electrical energy. Table 1 summarizes the characteristics of this solar cell with an efficiency of 17.1%.

TABLE 1 Characteristics of the SP5V400 solar cell

Power	2 W
Peak voltage	5 V
Open circuit voltage	6 V
Peak current	336 mA
Short circuit current	400 mA
Size	135 mm × 125 mm
Conversion efficiency	17.1 %

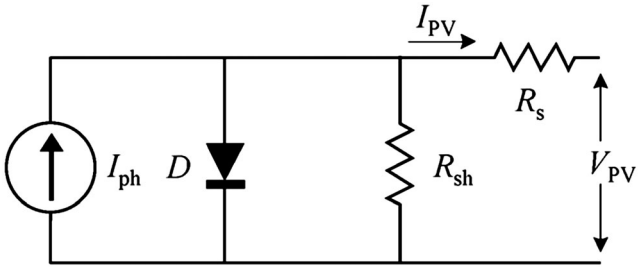

FIGURE 1 Electrical model for photovoltaic (PV) cell

Figure 1 shows a simple model of a PV cell. The mathematical relationships of such PV cell can be computed based on this model. Equation (1) can be used to calculate the I_{PV} current (excluding leakage current):

$$I_{PV} = I_{ph} - I_o\left[\exp\left(\frac{V_{PV} + I_{PV}.R_s}{V_t}\right) - 1\right], \quad (1)$$

where I_{ph} is the current produced by light (A), I_o is the reverse saturation current of p-n diodes (1×10^{-9} A), R_s is the series resistance of PV cell, and V_t is the thermal voltage of the connection terminal (V). Note that V_t depends on the absolute temperature of the cell, which is defined on (2):

$$V_t = \frac{kT_c}{q}, \quad (2)$$

where T_c is the cell absolute temperature (K), k is the Boltzmann constant ($1.3807 \times 10^{-23}\ JK^{-1}$), and q is the charge of the electron (1.6022×10^{-19} C). Accordingly, the PV power can be formulated as (3):

$$P_{PV} = V_{PV}.I_{PV} = V_{PV}\left[I_{ph} - I_o(e^{(\frac{V_{PV}+I_{PV}R_s}{kT_c/q})} - 1\right]. \quad (3)$$

According to a PV cell's current–voltage (I-V) and power–voltage (P-V) curves, there is a specific working voltage and current under a certain radiation and temperature that produces the maximum power of P_{max} [29]. It is necessary to experimentally measure the open circuit voltage (V_{OC}) and the short-circuit current (I_{SC}) to calculate the power of the MPP (P_{mpp}). This is called Pmpp, and this point is the product of the voltage of MPP (V_{mpp}) and the current of MPP (I_{mpp}). As depicted in Figure 2,

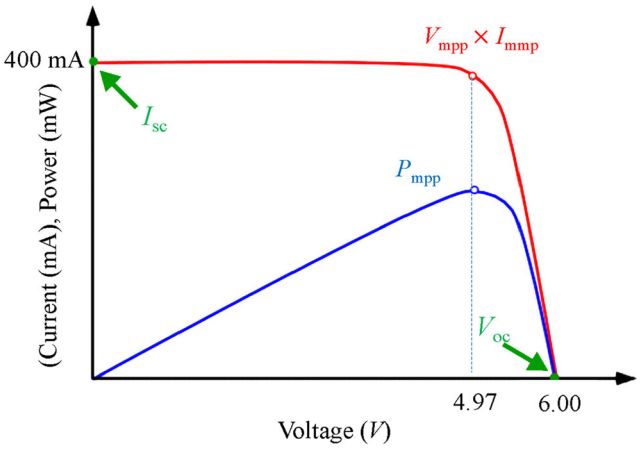

FIGURE 2 I-V and P-V curves of a photovoltaic (PV) cell (SP5V400)

the MPP of the PV cell is related to these specific operating voltage and current points.

2.2 | Thermoelectric EH system

One distinct approach to produce electrical energy is to use TEG, which works based on the temperature difference on its both sides [30]. TEG is a semiconductor device that converts temperature difference into electrical potential difference through the Seebeck effect [31]. As this temperature difference increases, the overall output voltage deliverable at the TEG's output will be higher. The proposed technique implemented in this paper recycles the heat across the body of the PV cell which otherwise would have been wasted. In other words, the temperature difference between the body of the PV cell and air (or the water in case of being used in the ocean) would be utilized to extract the energy of heated PV cells, while PV converts the incoming light into electricity. Since TEGs have a low-power density, their series and parallel connections can be configured to increase the received power [32]. The TEGs used in this paper have the part number of SP1848-27145. A series of five TEGs are attached to the body of the PV cells for implementation. In addition, the technique of placing heatsinks on the cold side of the TEGs is utilized to generate higher temperature difference leading to greater resultant voltage. These TEGs consist of thermal elements of N and P types, which are electrically connected in series and thermally in parallel [33]. The performance of thermoelectric elements for power generation and cooling is evaluated based on its competence figure known as ZT [34] given in (4),

$$ZT = \frac{\sigma\alpha^2}{k}T, \tag{4}$$

where α is the Seebeck coefficient, σ is the electrical conductivity, T is the absolute temperature, and k is the thermal conductivity. The performance of TEG improves with the ZT value. Therefore, it is preferable to choose TEG with a higher ZT value to accomplish a better performance [35]. Figure 3 shows a simple electrical model of the TEG that describes the mathematical equations.

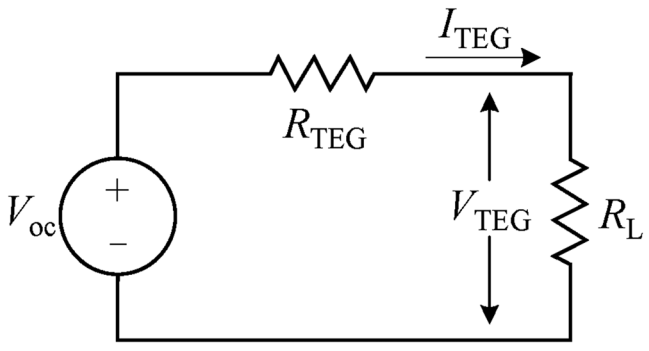

FIGURE 3 Electrical model for thermoelectric generator (TEG)

For a TEG that consists of n thermocouples, the V_{OC} open circuit voltage of the TEG is calculated as in (5):

$$V_{OC} = S \times \Delta T_{TEG} = n \times \alpha(T_{HJ} - T_{CJ}), \tag{5}$$

where α and S are the Seebeck coefficient of a thermocouple and a TEG, respectively. Besides, ΔT_{TEG} is the temperature difference and T_{HJ} and T_{CJ} are the temperatures of the hot and cold sides, respectively. In addition, (6) can be used to measure the current of TEG (I_{TEG}):

$$I_{TEG} = \frac{V_{OC}}{R_{TEG} + R_L}, \tag{6}$$

where R_{TEG} is the internal resistance of TEG and R_L is a load resistance that is connected to the TEG. In addition, value of R_{TEG} is given in (7):

$$R_{TEG} = \frac{L}{\sigma A_{leg}} + \frac{2L_C}{\sigma_C A_C}, \tag{7}$$

where σ_C is the contact electrical conductivity of the copper strip, A_{leg} is the cross-section area of thermoelectric elements, A_C is the cross-section area of the copper strip, L is the thermocouple length, and L_C is the length of copper strip. In addition, (8) can be used to calculate the power taken from TEG:

$$P_{TEG} = \frac{(V_{OC} \cdot \frac{R_L}{R_{TEG}+R_L})}{R_L} = \frac{\alpha^2 . \Delta T_{TEG}^2 . R_L}{R_{TEG} + R_L}. \tag{8}$$

The maximum power transfer from the TEG source to the load is obtained under the condition of $R_{TEG} = R_L$. To get the most power from the TEG, the MPPT approach can be implemented to match the impedance of the energy source to the load. Given that the load resistance is the same as the resistance of the collector source, the power taken is always maximum for various temperature differences [6].

2.3 | DC-to-DC converter for EH system

Due to the variability of electrical energy extracted from the PV cell and TEG in different climatic conditions, it is necessary to use DC converters to increase/decrease and

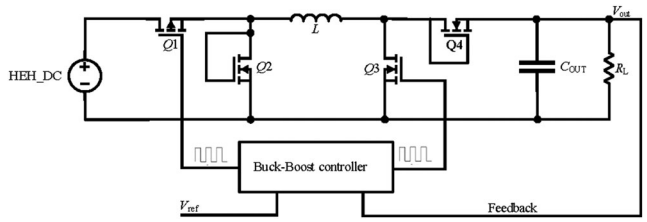

FIGURE 4 Structure of the non-inverting buck–boost converter

stabilize the voltage. Hence, in this paper, a non-inverting buck–boost converter is used to provide a constant and stabilized output voltage [36].

Figure 4 shows the structure of this buck–boost converter. In this circuit, instead of conventional rectifier diodes, the diode-connected Q2 and Q4 transistors are used to provide a low voltage drop. In this converter, TL494 is used to control the feedback loop.

Transistors Q1 and Q3 are turned ON and OFF by a control circuit via a pulse-width modulation (PWM) signal. Based on the comparison between the sampled output voltage and the reference voltage, when the input voltage is higher than the output voltage, the converter operates in buck mode. On the contrary, when the input voltage is less than the output voltage, the converter operates in boost mode [37, 38]. Moreover, the boost converter in EH systems can be fully integrated as a chip without the need of a coil. This is accomplished by the idea of the double boost converter [39].

The conversion ratio ($M(D)$) in the buck–boost converter is obtained from (9).

$$M(D)=\frac{V_{\text{out}}}{V_{\text{in}}}=\frac{V_{R_{\text{L}}}}{V_{\text{HEH-DC}}}=\frac{D}{1-D}. \tag{9}$$

Using the small-ripple approximation and writing KVL and KCL equations, the following are obtained [36]:

$$L\frac{d\hat{i}(t)}{dt}=D\hat{v}_g(t)-D'\hat{v}(t)+(V_g+V)\hat{d}(t), \tag{10}$$

$$C\frac{d\hat{v}(t)}{dt}=D'\hat{i}(t)-\frac{\hat{v}(t)}{R}-I_L\hat{d}(t), \tag{11}$$

$$\hat{i}_g(t)=D\hat{i}(t)+I\hat{d}(t), \tag{12}$$

where i is the inductor current and D is the duty cycle. The parameters $\hat{i}(t),\hat{v}_g(t),\hat{v}(t),\hat{d}(t)$, and $\hat{i}_g(t)$ are small-signal AC variations of inductor current, input voltage, output voltage, duty cycle, and input current, respectively.

According to these equations, the control-to-output transfer function is of the following form:

$$G_{vd}(s)=\frac{\hat{v}(s)}{\hat{d}(s)}=G_{d0}\frac{(1-\frac{s}{\omega_{zd}})}{(1+\frac{s}{Q\omega_0}+(\frac{s}{\omega_0})^2)}. \tag{13}$$

In addition, the line-to-output transfer function can be calculated as follows:

$$G_{vg}(s)=\frac{\hat{v}(s)}{\hat{v}_g(s)}=G_{g0}\frac{1}{1+\frac{s}{Q\omega_0}+(\frac{s}{\omega_0})^2}. \tag{14}$$

The parameters associated with this noninverting buck–boost converter is given in Table 2.

Equations (13) and (14) can be used to design the closed-loop system and to verify its stability.

The input voltage of the buck–boost converter (V_{in}) is taken from the hybrid energy harvester source (HEH-DC), as depicted in Figure 4. In this converter, the transistor IRF3205 is used for Q1 and Q3, and the transistor IRLZ44 is used for Q2 and Q4. In boost mode, the value of inductor (L) is formulated as in (15):

$$L=\frac{V_{\text{in(min)}}^2(V_{\text{out}}-V_{\text{in(min)}})}{0.2.I_{\text{out(max)}}.f_{\text{sw}}.V_{\text{out}}^2}, \tag{15}$$

where $I_{\text{out(max)}}$ is the maximum load current. In this design, Tmote Sky wireless sensor node is considered as the load, which requires a voltage of 3.3 V. In addition, f_{sw} is switching frequency set at 40 kHz supplied by the control circuit. Equation (16) can be used to calculate the saturation current of the inductor ($I_{\text{L(sat)}}$) rating at a minimum input voltage.

$$I_{\text{L(sat)}}\geq\times\left(\frac{V_{\text{out}}\times I_{\text{out(max)}}}{0.9\times V_{\text{in(min)}}}+\frac{\Delta I_{\text{L}}}{2}\right), \tag{16}$$

where ΔI_{L} is the inductor ripple current. A higher inductance provides smaller ripple current at the expense of the inductor size, cost, and DC resistance [40]. Besides, the output capacitor is chosen based on the maximum RMS current in the capacitor during boost mode and the output voltage ripple profile. When operating at the

TABLE 2 Parameters of the non-inverting buck–boost converter

G_{g0}	G_{d0}	ω_0	Q	ω_{zd}
$\frac{D}{D'}$	$\frac{V}{DD'}$	$\frac{D'}{\sqrt{LC}}$	$D'R\sqrt{\frac{C}{L}}$	$\frac{D'^2R}{DL}$

minimum input voltage and maximum load, the maximum RMS current in the output capacitor ($I_{C\text{out-rms}}$) can be obtained using (17).

$$I_{C\text{out-rms}} = I_{\text{out}} \times \sqrt{\frac{V_{\text{out}}}{V_{\text{in}}} - 1}. \tag{17}$$

The output ripple has components based on the equivalent series resistance (ESR) that represents the ESR-based ripple (ΔV_{ESR}) given in (18) and the capacitive ripple ($\Delta V_{C\text{out}}$) given in (19).

$$\Delta V_{\text{ESR}} = \frac{I_{\text{out}} \times V_{\text{out}}}{V_{\text{in(min)}}} \times \text{ESR}, \tag{18}$$

$$\Delta V_{C\text{out}} = \frac{I_{\text{out}}}{C_{\text{out}} \times f_{\text{sw}}} \times \left(\frac{V_{\text{out}} - V_{\text{in}}}{V_{\text{out}}}\right). \tag{19}$$

The maximum capacitive ripple occurs at the minimum input voltage. Moreover, the input capacitor can be selected in the same manner as the output capacitor. The maximum RMS current flowing in C_{in} occurs in buck mode given as follows:

$$I_{\text{Cin(rms)}} = I_{\text{out}} \times \sqrt{\frac{V_{\text{out}}}{V_{\text{in}}}\left(1 - \frac{V_{\text{out}}}{V_{\text{in}}}\right)}. \tag{20}$$

The input voltage ripple is a combination of capacitive and ESR-based ripple. The ESR-based ripple at the input can be calculated as follows:

$$\Delta V_{\text{Ripple(ESR)}} = I_{\text{out}}\text{ESR}. \tag{21}$$

In addition, the capacitive input ripple can be determined as follows:

$$\Delta V_{\text{Ripple}(C_{\text{in}})} = \frac{I_{\text{out}} \frac{V_{\text{out}}}{V_{\text{in}}} \times \left(1 - \frac{V_{\text{out}}}{V_{\text{in}}}\right)}{C_{\text{in}} f_{\text{sw}}}. \tag{22}$$

According to the abovementioned equations, the values of the inductor and capacitor are calculated to be $L = 470$ μH and $C = 82$ μF, and the value of the supercapacitor is 1 F.

The combination of energy sources at the input is one of the main challenges in HEH systems. A common technique is to use a diode block on the entrance floor. In this block, only the energy harvester can be used as the direct input of the converter, which has a higher voltage level. Due to the low harvested voltages, making a diode block with metal-oxide-semiconductor field effect transistor (MOSFET) (Figure 5) is recommended to approach the ideal diode structure. Although using a diode block is a common method of combining energy sources, a disadvantage is that only one of the inputs is connected to the output at a time. In other words, in a diode block structure, only one energy source is responsible for supplying the load at any given time. It is worth noting that separate supercapacitors can be used for each input to store the harvested energy permanently. Moreover, in case the input power sources have different impedances, the PWM signal generated by the control circuit should be programmed such that the impedance matching of the load and the source satisfied to maximize the output power. Since the conventional approach of using a diode block is not suitable for maximizing the output power, the method of applying the current mirror at the input stage is proposed in this paper and is described in the following section. The diode block can be used to provide the supply voltage needed for the battery-free operation of the current mirror, which is explained in the next section.

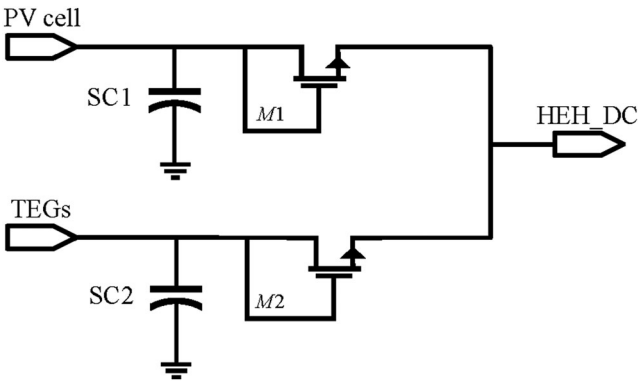

FIGURE 5 Diode connection with p-channel MOSFET (PMOS)

3 | PROPOSED METHOD OF COMBINING HARVESTED ENERGIES

In this paper, the main idea for combining energy sources in the input floor is based on using a current mirror circuit so that no energy source is left unused at any time. The current mirror is a circuit that is designed to copy the current through an active circuit by controlling the current in another circuit and keeping the output current constant regardless of the load [41]. To achieve this, two possible approaches are depicted in Figure 6, which shows the block diagrams of the suggested HEH systems.

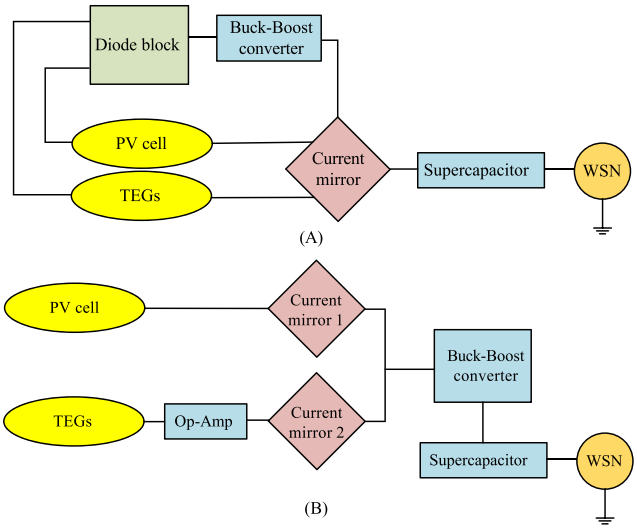

FIGURE 6 Suggested current mirror-based block diagrams of the HEH system: (A) Using a diode block; (B) using OpAmp

3.1 | Proposed circuit topologies

The goal is to increase the corresponding currents taken from environmental energy sources to achieve more power, and this is accomplished via a current mirror circuit. In Figure 6A, the input sources, that is, PV cell and TEGs, act as the inputs to the mirror current circuit and the inputs to the diode block. The diode block implemented with MOSFET transistors conveys the input with higher voltage to its output with the least voltage drop. Next, the output of this block is applied to a buck–boost converter to provide a suitable and stabilized voltage for the operation of the current mirror circuit. As is depicted in this figure, the output of the current mirror is connected to the supercapacitor to store the generated electrical energy continuously and supply the load. It is worth noting that in practice, the electrical energy produced by light is more than that of heat; therefore, to stabilize and regulate the voltage, the converter operates in the buck mode for the PV cell and in the boost mode for the TEGs. In Figure 6B, the input sources, that is, PV cell and TEGs, act as the inputs to the mirror current circuit. The diode block is not used in this scheme. Instead, an OpAmp is used to amplify the DC level of voltage excavated from the TEGs. This amplified voltage along with the voltage acquired from the PV cell is then applied to the current mirror cells. Next, the output of both current mirrors will sum up and will be stored to a capacitor to provide the input voltage for the converter. This voltage is then applied to a buck–boost converter to provide a suitable and stabilized voltage for the load.

Figure 7 shows the proposed current mirror circuit based on the block diagrams of Figure 6. In Figure 7A, in addition to the proper combination of energy harvesters, the current will be increased at the output. In this case, more power can be transferred to the load. The current of the current mirror circuit is supplied through ambient energies harvested from SEH and TEH. In addition, OpAmp OP07 is used to elevate the level of output voltage delivered by the TEGs by the ratio of (1+R4/R3). Moreover, the transistor M1 is used to convert the voltage into a current, and no external power supply is required in the proposed current mirror circuit. In parallel, the highest harvested energy from SEH and TEH is passed through a diode block, and the corresponding voltage is then applied to the buck–boost converter to stabilize the voltage needed for the operation of the circuit. In proportion to the current of ambient energy sources, the resistors $R_{1,2}$ can be adjusted according to (23), along with the *I-V* equation of the MOS transistor,

$$I_{\mathrm{REF}} = \frac{V((\text{ambient source}) - V_{gs_n}}{R_{1,2}}, \tag{23}$$

where I_{REF} is I_{R1} (I_{R2}), which is the current of transistor M1 (M4), provided that SEH (TEH, i.e., Vin-TEG in Figure 7A) is used as the ambient energy source, R1 (R2) is used as resistor $R_{1,2}$, and $V_{gs,n}$ is used as gate-source voltage of M1(M4). As the TEH has a lower harvested energy compared to the SEH, regardless of its early amplification via the OpAmp, the current generated in the mirror circuit of a thermal source is multiplied by three, producing $I_y = 3 \times I_{R2}$, while the current generated in the mirror circuit of a solar source is multiplied by two, producing $I_X = 2 \times I_{R1}$. As a result, both currents are added together and transferred to the output as is expressed in (24). However, based on the nature of the load, any other multiplication factor of energy sources is applicable based on this proposed circuit. Using a similar transistor in the current mirror, the resultant current deliverable to the load is given in (25), as the p-channel MOSFET transistors M8 and M9 are also identical. Therefore, for discrete transistors which are bought off the shelf, the value of the aspect ratio, width to the length of transistors, is fixed.

$$I = I_x + I_y = 2I_{R_1}\left(\frac{(W/L)_{2,3}}{(W/L)_1}\right) + 3I_{R_2}\left(\frac{(W/L)_{5,6,7}}{(W/L)_4}\right), \tag{24}$$

$$I = 2I_{R_1} + 3I_{R_2}. \tag{25}$$

Given that this is a lossy implementation due to M8 and M9 transistors, the second implementation is

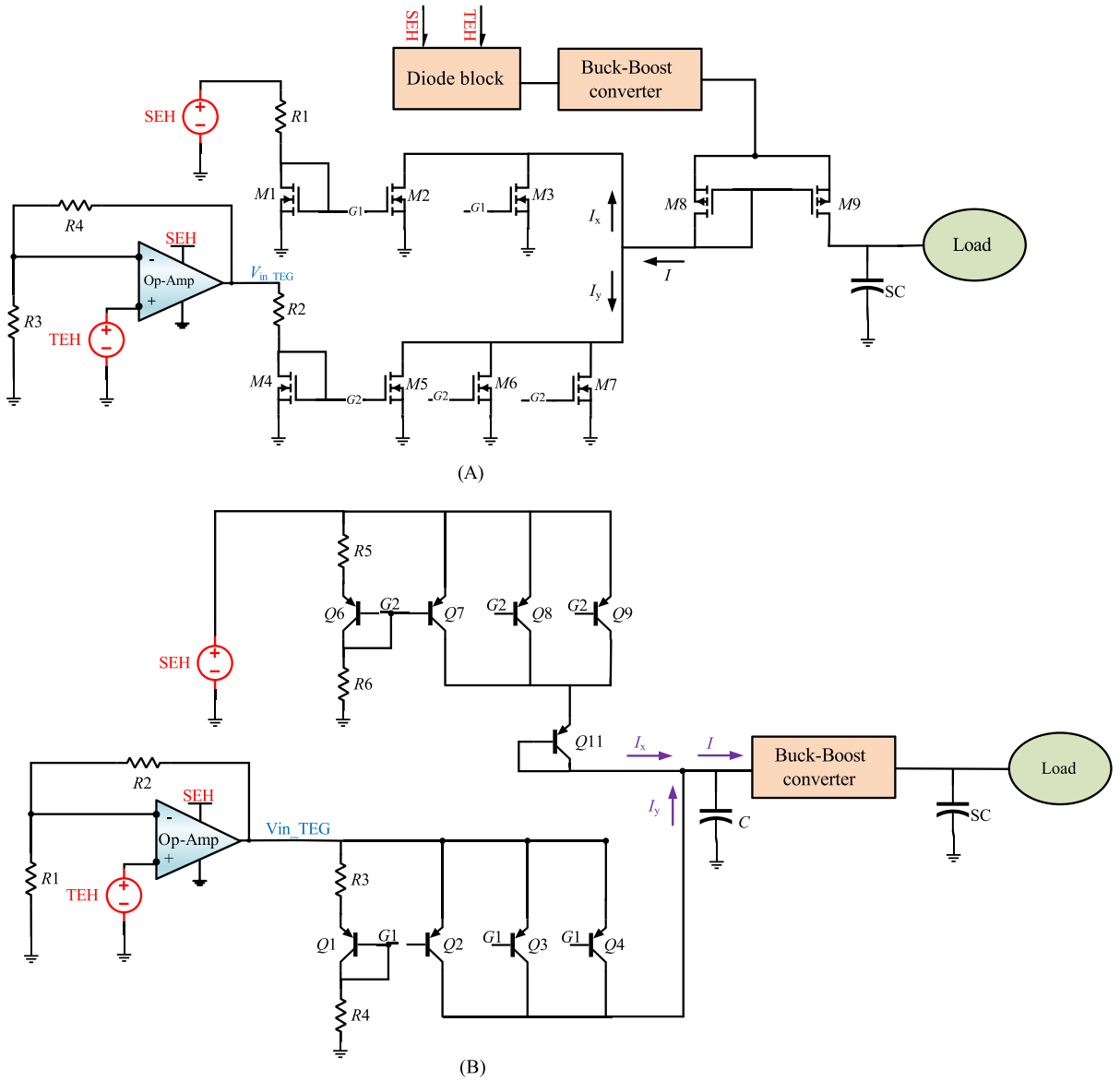

FIGURE 7 Proposed current mirror circuit: (A) standard current mirror, leading to high-power dissipation and (B) Widlar current mirror offering a higher efficiency compared with (A)

proposed, as depicted in Figure 7B. Two Widlar current sources are used in this circuit. The advantage of a Widlar circuit is that approximately small constant currents would be generated using small resistors. Indeed, small resistors provide low-enough power consumption compared with the current mirror structure of Figure 7A.

The input current due to the ambient energy sources can be reported approximately as (26) ignoring the base currents:

$$I_{\mathrm{REF}} = \frac{V(\text{ambient source}) - V_{\mathrm{EB}}}{R}, \tag{26}$$

where I_{REF} is I_{R5} (I_{R3}), which is the current of transistor Q6 (Q1), and V_{EB} is the emitter-base voltage of Q6 (Q1) provided that SEH (TEH, i.e., Vin-TEG in Figure 7B) is used as the ambient energy source. In this equation, resistance R is $R5+R6$ and $R3+R4$ for Q6 and Q1, respectively. OpAmp (OP07) is used in the same manner as in Figure 7A. The current I_y and I_x can be obtained from the following equations:

$$I_y = I_{C,2} + I_{C,3} + I_{C,4}, \tag{27}$$

$$I_x = I_{C,7} + I_{C,8} + I_{C,9}. \tag{28}$$

Transistors Q2, Q3, and Q4 have the same currents, which can be described as follows:

$$V_{EB1} = V_t \ln\left(\frac{I_{REF}}{I_s}\right), V_{EB2} = V_t \ln\left(\frac{I_{C2}}{I_s}\right). \quad (29)$$

Writing the KVL and KCL equations for this circuit, (30) is derived as follows:

$$V_{EB2} - V_{EB1} = R3 \times I_{REF} = V_t \ln\left(\frac{I_{C2}}{I_{REF}}\right), \quad (30)$$

where V_t is the thermal voltage and I_s is reverse saturation current of base-emitter diode. The current of Q7 can be calculated in the same manner as in (30). In addition, (27) and (28) can be simplified as $I_y = 3 \times I_{C2}$ and $I_X = 3 \times I_{C7}$, where I_{C2} and I_{C7} are the current of Q2 and Q7 transistors, respectively, derived from (30).

3.2 | Effect of nonidealities in the current mirror circuit

Regardless of its terminal voltage, an ideal current source can deliver different amounts of current. However, in practice, the load requirements also affect the value of constant current. Accordingly, the output voltage and the output current will change. Likewise, for a practical current source, the output impedance is not infinite, which by itself will limit the amount of output current. Indeed, some nonidealities, such as process variation, V_{DS} difference, and V_{TH} mismatch, may cause current mismatches.

Mismatch due to the threshold voltage: One of the mismatch factors in current mirror circuits is related to the threshold voltage, V_{TH}. Considering the nominally identical current sources M1 and M2 in Figure 8 and neglecting channel length modulation, the total mismatch between I_{D1} and I_{D2} can be determined as follows [42]:

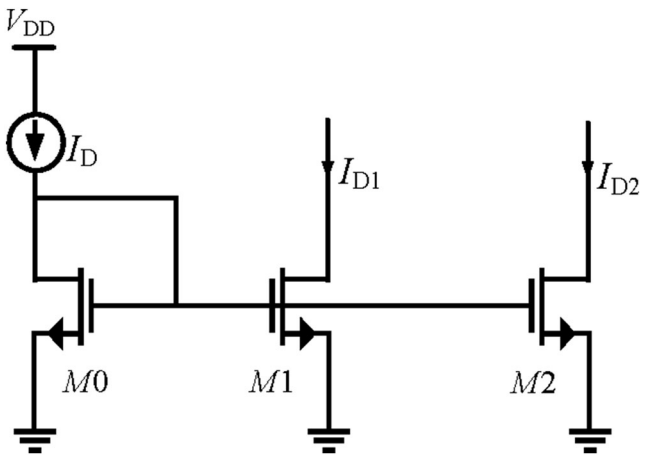

FIGURE 8 Mismatch between two current sources

Since $I_D = (1/2)\mu_n C_{ox}(W/L)(V_{GS} - V_{TH})^2$, the following is obtained:

$$\Delta I_D = \frac{\partial I_D}{\partial W/L}\Delta\frac{\partial W}{\partial L} + \frac{\partial I_D}{\partial (V_{GS} - V_{TH})}\Delta(V_{GS} - V_{TH}), \quad (31)$$

where mismatches in $\mu_n C_{ox}$ are neglected. It follows that

$$\Delta I_D = \frac{1}{2}\mu_n C_{ox}(V_{GS} - V_{TH})^2 \Delta\frac{\partial W}{\partial L} - \mu_n C_{ox}\frac{\partial W}{\partial L}(V_{GS} - V_{TH})\Delta V_{TH}. \quad (32)$$

It is worth noting that the current mismatch is usually normalized to the average value to allow a meaningful comparison:

$$\frac{\partial \Delta I_D}{\partial I_D} = \frac{\partial \Delta(W/L)}{\partial W/L} - 2\frac{\partial \Delta V_{TH}}{\partial V_{GS} - V_{TH}}. \quad (33)$$

This result suggests that, to minimize current mismatch, the overdrive voltage, $V_{GS} - V_{TH}$, must be maximized. This is because as $V_{GS} - V_{TH}$ increases, the threshold mismatch has a lesser effect on the device currents. In the same manner, it can be proved that

$$\frac{I_o}{I_{REF}} \approx 1 - \frac{2\Delta V_{THN}}{V_{GS} - V_{TH}} = 1 - \frac{2\Delta V_{THN}}{V_{DS,sat}}. \quad (34)$$

Equation (34) is quite noticeable since it shows that as V_{GS} decreases, the difference in the mirrored currents increases due to threshold voltage mismatch.

Mismatch due to the drain-to-source voltage and lambda: Both the matching in the drain-to-source voltages (V_o and V_{DS1}) and the device lambda (λ) affect the ratio of the output current to the reference current:

$$\frac{I_o}{I_{REF}} = \frac{1 + \lambda_2 V_o}{1 + \lambda_1 V_{DS1}}. \quad (35)$$

For good matching, it is extremely important that the V_{DS} values of the MOSFETs in the current mirror are equal. Given that channel length modulation is not considered ($\lambda = 0$), the ratio of currents is equal to the ratio of widths of transistors. However, according to the aforementioned equation, if two identical transistors do not have the same V_{DS}, then a nonlinearity related to the inequalities in λ and V_{DS} of transistors will occur in copying or mirroring the current provided by this equation.

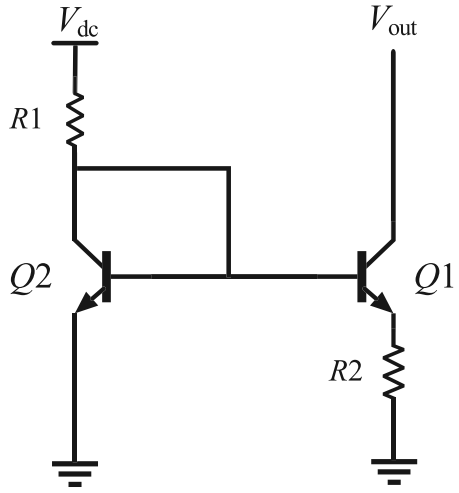

FIGURE 9 Widlar current mirror circuit

As mentioned earlier, the limited output resistance can also affect the operation of the current mirror. It is desired to have approximately infinite output resistance which is not feasible in practice. As a case in point, for the Widlar current mirror depicted in Figure 9, the output resistance is calculated as follows:

$$R_o = \frac{V_x}{I_x} = r_o\left(1+\frac{\beta R_2}{(R_1||r_e)+R_x+R_2}\right)+R_2\left(\frac{(R_1||r_e)+R_x}{(R_1||r_e)+R_x+R_2}\right), \tag{36}$$

where r_o is the intrinsic output resistance of the transistor, r_e is the intrinsic emitter resistance of a transistor, and R_x is the parasitic resistance at the base terminal. This value is way higher than the output resistance of simple current mirrors.

3.3 | Requirements of a supercapacitor

Recent research in EH systems utilizes supercapacitors as the promising source of energy storage. In an EH system, a supercapacitor is connected to the output of a DC-to-DC converter. Indeed, charging of supercapacitor with the converter circuit is preferred compared to charging directly with a rectifier. To select the appropriate supercapacitor for an EH application, a number of basic requirements, including the normal and minimum operating voltage, load current or its associated power, and duration of driving the load, should be taken into account.

The power that an ambient energy harvester can produce might not be high enough; however, the harvested energy can be continuously added into an energy storage device such as a battery or a supercapacitor to meet the needs of the load [43]. The total number of recharge cycles for the lifetime of a Li-battery is several hundreds. On the other hand, a normal supercapacitor will have millions of charge cycles, giving it a significant advantage as an energy storage solution. Moreover, if the leakage current of a supercapacitor is low and not the source of concern, a supercapacitor alone can be used as the storage device in indoor PV EH applications without the need of a battery. It is worth noting that self-discharge has been the primary concern for using the supercapacitors as the only storage component in sub-mW indoor PV EH applications for battery replacement solutions. This is mainly due to the difficulty in evaluating the energy loss in the charge redistribution process. In Yue and others [43], a charge-based storage evaluation method is presented to be used when the power management strategy is focused on maintaining charge stored in the supercapacitor to ensure that the total charge to the supercapacitor is not smaller than the total discharge.

The supercapacitor dynamics can also be modeled through an equivalent circuit formed by a capacitor connected in series with a resistance. Based on this model, the terminal voltage, V_{SC}, and the cell voltage can be formulated as follows [44, 45]:

$$V_{SC} = V_{OSC}(t) - R_{SC}I_{SC}(t), \tag{37}$$

$$V_{OSC} = V_{iC} - (1/C_{SC})\int_0^t I_{SC}dt, \tag{38}$$

where C_{SC} is the capacitance of the SC cell and V_{iC} is the initial voltage of supercapacitor. The SC cell current, I_{SC}, in terms of total absorbed/delivered power, P_{SC}, cell voltage, V_{OSC}, cell resistance, R_{SC}, and the total number of cells, n_{SC}, can be represented as follows:

$$I_{SC} = \frac{V_{OSC}(t)}{2R_{SC}} - \frac{\sqrt{V_{OSC}^2(t) - 4R_{SC}P_{SC}(t)/n_{SC}}}{2R_{SC}}. \tag{39}$$

4 | EXPERIMENTAL RESULTS

In this paper, five TEGs with the model number of SP1848-27145 were connected in series. In addition, their cold side is connected to the heatsink, and the hot side is connected to the back of the PV cell. In this case, as solar energy is converted into electrical energy, the heat generated on the cell is reused and converted into electrical energy as well. Based on the obtained experimental results, Table 3 presents the electrical energy generated by SP5V400, and Table 4 presents the electrical energy

generated by SP1848-27145 in different temperature and environmental conditions. In an open environment, the output power can be determined based on the temperature difference between the heat generated in the body of the PV cells and the air.

Figure 10 shows the power taken from one to five TEGs placed in series with different temperature variations. As it was expected, a larger number of TEGs should be hired to acquire higher harvested power.

All of five TEGs offer 0.9 V which will be amplified to 2.7 V via the OP07 OpAmp having R1 = 5 kΩ and R2 = 10 kΩ. Moreover, the output voltage of 4.9 V is also accessible from the solar cell. In addition, for the buck–boost converter, the values of the inductor and capacitor are chosen to be $L = 470$ μH and $C = 82$ μF, and the value of the supercapacitor (SC) is 1 F with a nominal voltage of 5.5 V. The SC with KAMCAP model is used here as a means of storing the excavated voltage deliverable to the load.

The resistors R3 to R6 were determined to control the current based on the requirements of the load according to (22) to the values of R3,5 = 22 Ω R4 = 1.9 kΩ and R6 = 2.2 kΩ. It is worth noting that all transistors are PNP type and have the part number 2N3906.

In this design, the current mirror circuit receives its power supply from the ambient energy sources, as depicted in Figure 6, and does not require an external power supply.

The input power is equal to the sum of the SEH and TEH powers, which is calculated to be 194 mW, and the power deliverable to the load is equal to 141 mW. Accordingly, the efficiency is calculated as (40):

$$\eta_{\%} = \frac{\text{OutputPower}}{\text{InputPower}} = \frac{141\ \text{mW}}{194\ \text{mW}} = 73\%. \qquad (40)$$

Figure 11 shows the output voltage of the buck–boost converter. The electrical energy obtained for normal use is stored in a 1 F SC.

Figure 12 shows a comparison between three EH techniques, namely, solar, thermal, and hybrid. In this scheme, the output power of five TEGs is equal to 72 mW, and the solar power output from a PV cell is equal to 122 mW. Thus, the structure of HEH provides 194 mW of power. The generated electrical energy is first stored in the supercapacitor and then transferred to the load. It is worth noting that this setup is solely a proof of concept for the idea of combing the energy sources via the current mirror cells, and surely higher output powers are accessible either by using larger PV cell or higher number of TEGs and temperature difference.

Figure 13 illustrates the experimental setup. It is supposed to power a Tmote Sky wireless sensor module with a 3.3 V power supply, and the maximum data transfer current is 23 mA for the receive mode and 21 mA for the transmit mode (overall maximum data transfer current of

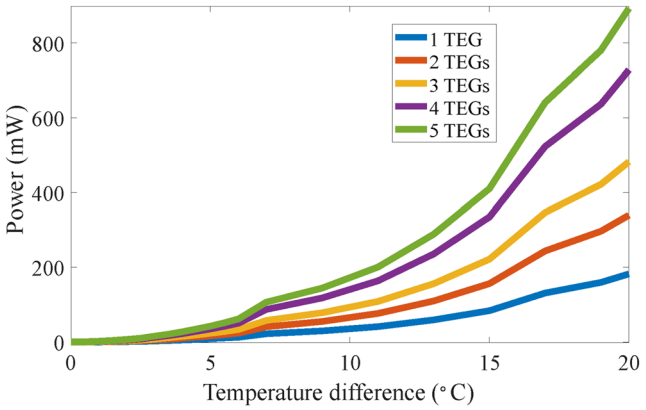

FIGURE 10 Input power received from one to five thermoelectric generators (TEGs)

TABLE 3 Experimental results obtained from PV cells

Sunny day	5 V
Cloudy day	3.5 V–3.7 V
Indoor light	3.0 V–3.4 V

Abbreviation: PV, photovoltaic.

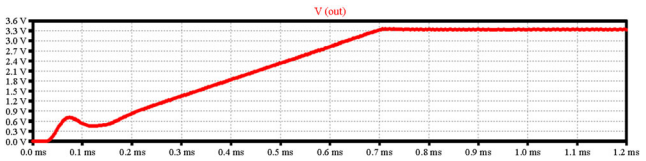

FIGURE 11 Buck–boost converter output voltage

TABLE 4 Experimental results obtained from a TEG

Temperature difference (° C)	3	5	7	9	11	13
Open circuit output voltage (V)	0.14	0.23	0.33	0.4	0.48	0.57
Output current (mA)	22.4	48.2	66	73.6	85.2	103.4

Abbreviation: TEG, thermoelectric generator.

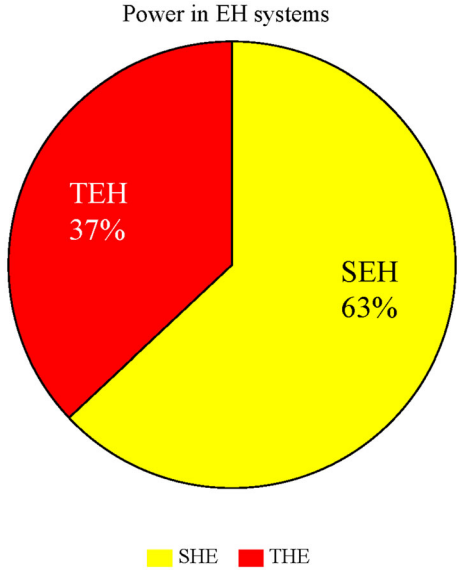

FIGURE 12 Input power received from one to four thermoelectric generators (TEGs)

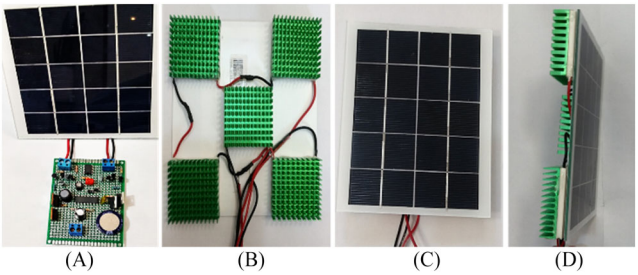

FIGURE 13 (A) Overall view of the proposed energy harvesting (HEH) system. (B) Connection of five thermoelectric generators (TEGs) to the photovoltaic (PV) cell. (C) PV cell appearance. (D) Both sides of the PV cell

44 mA). Depending on the size of the PV cell, more TEGs can be installed to receive more power from the TEGs. Given that the supercapacitors are fully charged, the power that the proposed HEH system can deliver to the wireless sensor module is equal to 141 mW.

The standard solar panel structure has a lower implementation cost compared with the proposed structure; however, its efficiency is significantly reduced. In this case, if a higher value solar cell is used as the input without TEGs, the efficiency will increase; however, it is still lower than the efficiency of the proposed structure, and the thermal energy can no longer be used to guarantee the continuous supply of electrical energy. Table 5 presents the comparison between the standard solar panel and the proposed system in terms of cost and efficiency.

TABLE 5 Comparison of efficiency and cost of different structures of EH systems

Circuit structure	Cost ($)	Efficiency
Proposed structure (1 solar panel + 5 TEGs)	15.28	73%
Standard solar panel (1 solar cell without TEGs)	5.18	36%
2 parallel solar cell circuits	8.36	69.5%

Abbreviations: EH, energy harvesting; TEG, thermoelectric generator.

As presented in Table 5, the cost of the proposed system, that is, $15.28, is higher compared with the other two systems not having the TEGs. However, due to the structure of the Widlar current mirror providing current with small value resistors, the proposed design provides higher efficiency which is 73%.

5 | CONCLUSION

This paper reports a methodology for combining the extracted energies from different environmental sources, for example, solar and thermal. This is achieved via implementation of a current mirror structure at the input stage to convert the associated received voltages into currents and then scale and sum them together using circuit techniques. This is indeed an HEH system composed of solar cell and TEGs proposed to combine all incoming energies concurrently to power the load which is considered to be a wireless sensor node. To increase the voltage level produced by TEG, five TEGs on the back of the PV cell were utilized to reuse the natural heat at the surface of PV cell. In addition, a buck–boost converter is used to adjust and stabilize the supply of the circuit. In this system, the excess electrical energy in the environment is continuously stored in the supercapacitor, which alone can supply the load.

ACKNOWLEDGMENTS

The authors would like to acknowledge the financial support from Ministry of Science, Research, and Technology as well as the Information and Communication Technology Park, Iran, for this project under grant number 32-00-01-000456.

CONFLICT OF INTEREST

The authors declare that there are no conflicts of interest.

ORCID

Mostafa Noohi https://orcid.org/0000-0002-8974-3155

REFERENCES

1. Y. Chen, *Communications, energy harvesting: principles and theories*, John Wiley and Sons, 2019.
2. S. M. Demir, F. Al-Turjman, and A. Muhtarolu, *Energy scavenging methods for WBAN applications: A review*, IEEE Sensors J. **18** (2018), no. 16, 6477–6488.
3. S. E. Moon, *Sustainable vibration energy harvesting based on Zr doped PMN-PT piezoelectric single crystal cantilevers*, ETRI J. **31** (2009), no. 6, 688–694.
4. M. Dezyani, H. Ghafoorifard, S. Sheikhaei, and W. A. Serdijn, *A 60 mV input voltage, process tolerant start-up system for thermoelectric energy harvesting*, IEEE Trans. Circ. Syst. I: Reg. Pap. **65** (2018), no. 10, 3568–3577.
5. R. Ibrahim, T. D. Chung, S. M. Hassan, K. Bingi, and S. K. Salahuddin, *Solar energy harvester for industrial wireless sensor nodes*, Procedia Comput. Sci. **105** (2017), 111–118.
6. Y. K. Tan, *Energy harvesting autonomous sensor systems: design, analysis, and practical implementation*, CRC Press, 2013.
7. M. Piuela, P. D. Mitcheson, and S. Lucyszyn, *Ambient RF energy harvesting in urban and semi-urban environments*, IEEE Trans. Microw. Theory Tech. **61** (2013), no. 7, 2715–2726.
8. S. E. Moon, *Sustainable vibration energy harvesting based on Zr-doped PMN-PT piezoelectric single crystal cantilevers*, ETRI J. **31** (2009), no. 6, 688–694.
9. S. Kosunalp, *MAC protocols for energy harvesting wireless sensor networks: Survey*, ETRI J. **37** (2015), no. 4, 804–812.
10. N. Rouibah, L. Barazane, M. Benghanem, and A. Mellit, *IoT-based low-cost prototype for online monitoring of maximum output power of domestic photovoltaic systems*, ETRI J. **43** (2021), no. 3, 459–470.
11. J. Yan, X. Liao, S. Ji, and S. Zhang, *A novel multi-source micro power generator for harvesting thermal and optical energy*, IEEE Electr. Device Lett. **40** (2018), no. 2, 349–352.
12. R. Komiyama and Y. Fujii, *Analysis of energy saving and environmental characteristics of electric vehicles in regionally disaggregated world energy model*, Electr. Eng. Japan **186** (2014), no. 4, 20–36.
13. R. Torah, P. Glynne-Jones, M. Tudor, T. O'donnell, S. Roy, and S. Beeby, *Self-powered autonomous wireless sensor node using vibration energy harvesting*, Meas Sci Technol **19** (2008), no. 12, 125202.
14. S. Heo, Y. S. Yang, J. Lee, S. k. Lee, and J. Kim, *Efficient maximum power tracking of energy harvesting using a μcontroller for power savings*, ETRI J. **33** (2011), no. 6, 973–976.
15. Y. Tadesse, S. Zhang, and S. Priya, *Multimodal energy harvesting system: Piezoelectric and electromagnetic*, J. Intell. Mater. Syst. Struct. **20** (2009), no. 5, 625–632.
16. A. Khaligh, P. Zeng, and C. Zheng, *Kinetic energy harvesting using piezoelectric and electromagnetic technologies state of the art*, IEEE Trans. Ind. Electr. **57** (2009), no. 3, 850–860.
17. N. J. Guilar, T. J. Kleeburg, A. Chen, D. R. Yankelevich, and R. Amirtharajah, *Integrated solar energy harvesting and storage*, IEEE Trans. Very Large Scale Integr. (VLSI) Syst. **17** (2009), no. 5, 627–637.
18. H. Lhermet, C. Condemine, M. Plissonnier, R. Salot, P. Audebert, and M. Rosset, *Efficient power management circuit: From thermal energy harvesting to above-IC microbattery energy storage*, IEEE J. Solid-State Circuits **43** (2008), no. 1, 246–255.
19. T. N. T. Mohamad, J. Sampe, and D. D. Berhanuddin, *Architecture of micro energy harvesting using hybrid input of RF, thermal and vibration for semi-active RFID tag*, Eng. J. **21** (2017), no. 2, 183–197.
20. W.-K. Lee, M. J. Schubert, B.-Y. Ooi, and S. J.-Q. Ho, *Multi-source energy harvesting and storage for floating wireless sensor network nodes with long range communication capability*, IEEE Trans. Ind. Appl. **54** (2018), no. 3, 2606–2615.
21. Y. K. Tan and S. K. Panda, *Energy harvesting from hybrid indoor ambient light and thermal energy sources for enhanced performance of wireless sensor nodes*, IEEE Trans. Ind. Electron. **58** (2010), no. 9, 4424–4435.
22. T. Kang, S. Kim, C. Hyoung, S. Kang, and K. Park, *An energy combiner for a multi-input energy-harvesting system*, IEEE Trans. Circ. Syst. II: Express Briefs **62** (2015), no. 9, 911–915.
23. D. Altinel and G. K. Kurt, *Modeling of multiple energy sources for hybrid energy harvesting IoT systems*, IEEE Internet Things J. **6** (2019), no. 6, 10846–10854.
24. T. Tanaka, T. Aonuma, K. Natori, and Y. Sato, *Rectification methods to increase harvested energy in vibration generation using piezoelectric elements*, Electr. Eng. Japan **199** (2017), no. 3, 68–79.
25. F. Deng, X. Yue, X. Fan, S. Guan, Y. Xu, and J. Chen, *Multisource energy harvesting system for a wireless sensor network node in the field environment*, IEEE Internet Things J. **6** (2018), no. 1, 918–927.
26. I. G. Zurbriggen and M. Ordonez, *PV energy harvesting under extremely fast changing irradiance: State-plane direct MPPT*, IEEE Trans. Ind. Electron. **66** (2018), no. 3, 1852–1861.
27. A. Decker, *Solar energy harvesting for autonomous field devices*, IET Wireless Sensor Syst. **4** (2013), no. 1, 1–8.
28. S. Sharma, K. K. Jain, and A. Sharma, *Solar cells: in research and applications: A review*, Mater. Sci. Appl. **6** (2015), no. 12, 1145.
29. T. Esram and P. L. Chapman, *Comparison of photovoltaic array maximum power point tracking techniques*, IEEE Trans. Energy Convers. **22** (2007), no. 2, 439–449.
30. M. Dezyani, H. Ghafoorifard, S. Sheikhaei, and W. A. Serdijn, *A 60 mV input voltage, process tolerant start-up system for thermoelectric energy harvesting*, IEEE Trans. Circ. Syst. I: Reg. Pap. **65** (2018), no. 10, 3568–3577.
31. J. Kim, *Dynamic reconfiguration of thermoelectric generators for vehicle radiators energy harvesting under location-dependent temperature variations*, IEEE Trans. Very Large Scale Integr. (VLSI) Syst. **26** (2018), no. 7, 1241–1253.
32. L. Sigrist, N. Stricker, D. Bernath, J. Beutel, and L. Thiele, *Thermoelectric energy harvesting from gradients in the Earth surface*, IEEE Trans. Ind. Electron. **67** (2019), no. 11, 9460–9470.
33. D. Enescu, *Thermoelectric energy harvesting: Basic principles and applications, Green Energy Advances, London, United Kingdom*, IntechOpen, (2019). https://www.intechopen.com/chapters/65239, https://doi.org/10.5772/intechopen.83495
34. Y. Wu, Thermoelectric Energy Harvesting for Sensor Powering Virginia Tech, 2019.
35. J. Yan, X. Liao, D. Yan, and Y. Chen, *Review of micro thermoelectric generator*, J. Microelectromech. Syst. **27** (2018), no. 1, 1–18.

36. R. W. Erickson and D. Maksimovic, *Fundamentals of power electronics*, Springer Science and Business Media, 2007.
37. W.-Z. Zhang, H.-P. Lin, Y. Zhang, and J.-M. Jin, *Modeling and controlling strategy of four-switch buck-boost convertor with smooth mode transitions*, Open Electr. Electr. Eng. J. **11** (2017), 1.
38. J.-H. Park, H. Kim, and H.-J. Kim, *A current-mode non-inverting CMOS buck-boost DC-DC converter* (INTELEC 2009-31st International Telecommunications Energy Conference, Incheon, Rep. of Korea), 2009.
39. A. Uemi, S. Hino, and Y. Masui, *Low-voltage charge pump circuit with double boost technique*, Electr. Eng. Japan **213** (2020), no. 1-4, 24–32.
40. V. Choudhary, T. Hegarty, and D. Pace, Under the hood of a non-inverting buck-boost converter in Texas Instruments Power Supply Design Seminar, 2017.
41. K. Kubota and M. Okine, *Realization of a multiport gyrator using current mirror circuits*, Electr. Eng. Japan **139** (2002), no. 4, 41–47.
42. B. Razavi, *Design of analog CMOS integrated circuits*, Second edition, McGraw-Hill Education, 2017.
43. X. Yue, J. Kiely, D. Gibson, and E. M. Drakakis, *Charge-Based supercapacitor storage estimation for indoor sub-mW Photovoltaic energy harvesting powered wireless sensor nodes*, IEEE Trans. Ind. Electr. **67** (2020), no. 3, 2411–2421.
44. J. Nunez Forestieri and M. Farasat, *Integrative sizing/real-time energy management of a hybrid supercapacitor/undersea energy storage system for grid integration of wave energy conversion systems*, IEEE J. Emerg. Sel. Top. Power Electr. **8** (2020), no. 4, 3798–3810.
45. S. Lee and J. Kim, *Power capability analysis of lithium battery and supercapacitor by pulse duration*. Electronics. **8** (2019), no. 12, 1395.

AUTHOR BIOGRAPHIES

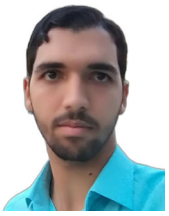

Mostafa Noohi received his BS degree in Electrical Engineering from Shahid Bahonar College, Shiraz, Iran, in 2018, and MS degree in Electrical Engineering from Yazd University, Yazd, Iran, in 2021. He is currently pursuing his PhD degree in Electrical Engineering at Sahand University of Technology, East Azerbaijan, Sahand, Iran. His research interests include hybrid energy harvesting, RF, computer-aided design, and artificial intelligence.

Ali Mirvakili received his BS degree in Electronics Engineering from Yazd University, Yazd, Iran, in 2005, his MS degree from K.N. Toosi University of Technology, Tehran, Iran, in 2008, and his PhD degree from Tufts University, Medford, MA, USA, in 2014. He was at Advanced Integrated Circuits and Systems Lab. and student member of Smart Lighting Engineering Research Center, Tufts University, Medford, MA, USA, from 2010 to 2014, where he worked on LED Driver Architecture Design and Tesbed Integration for Visible Light Communication (VLC). He was electronics and programming intern at Osram Sylvania, Wilmington, MA, USA, from 2014 to 2015, and electrical design engineer at Sensata Technologies, Attleboro, MA, USA, from 2015 to 2016. He joined the Department of Electrical Engineering at Yazd University, Yazd, Iran, in 2016 as assistant professor. His research interests include power management for energy harvesting, VLSI, RF, and mixed-signal circuit design for VLC and biomedical applications and DC-to-DC converter control.

Hadi Safdarkhani received his BS, MS, and PhD degrees in Electrical Engineering from Amirkabir University of Technology, Tehran, Iran, in 2005, 2008, and 2015, respectively. He is currently an assistant professor in the Department of Electrical Engineering, Yazd University, Yazd, Iran. His research interests include analog and digital system analysis and design, the IoT, and industrial networks. Dr. Safdarkhani has been the chair of Intelligent Systems Research Institute, Yazd University, Yazd, Iran, since 2019, where several research groups have been working on areas such as mechatronics, signal processing, telecommunication, and computer networks.

Sayed Alireza Sadrossadat (Member, IEEE) received his BS degree from the University of Tehran, Tehran, Iran, in 2007, his MS degree from the University of Waterloo, Waterloo, ON, Canada, in 2010, and his PhD degree from Carleton University, Ottawa, ON, Canada, in 2015. He is currently the chair of the Artificial Intelligence Group, Department of Computer Engineering, Yazd University, Yazd, Iran. His current research interests include neural network-based modeling and optimization of linear/nonlinear components, computer-aided design, very large-scale integration systems and probabilistic design, and yield maximization. Dr. Sadrossadat has been a technical reviewer for several IEEE/IET journals, such as IEEE Transactions on Neural Network and Learning Systems, IEEE Transactions on Microwave Theory and Technique, IEEE Transactions on

Very Large-Scale Integration Systems, IET Microwave and Propagation, IET Electronic Letters, and IEEE Canadian Journal of Electrical and Computer Engineering.

How to cite this article: M. Noohi, A. Mirvakili, H. Safdarkhani, and S. A. Sadrossadat, *Thermally reused solar energy harvesting using current mirror cells*, ETRI Journal **45** (2023), 519–533. https://doi.org/10.4218/etrij.2022-0011